出國報告（出國類別：實習）

赴美國俄亥俄州立大學(The Ohio State University)實習核能組件銲接修補技術案

服務機關：核能研究所
姓名職稱：鄭勝隆　工程師
派赴國家：美國
出國期間：104 年 6 月 18 日~104 年 9 月 28 日
報告日期：104 年 10 月 28 日

摘要

此行為前往美國俄亥俄州立大學材料科學與工程學系的銲接學程(welding program)，實習 Strain to Fracture (STF)實驗，用以評估鎳基合金失延裂紋(Ductility Dip Cracking, DDC) 的敏感性。在實習期間，同時也參觀該學程的 Cast Pin Tear Test 及 Varstrain Test 等兩種熱裂測試設備，參觀以 SS-DTA 技術量測材料相變化溫度的實驗，並了解該學程購置的 Thermal Cal. 及 JMetPro 等兩種材料軟體的使用情形。

STF 的測試結果顯示，若選用 308L 為緩衝層材料時，發生 DDC 的應變門檻值約在 9.8%；若採用 307Si 及 347 不銹鋼為緩衝層材料時，可以分別提高 DDC 的應變門檻值至 11.1%及 13.3%；若選用 316L 為緩衝層材料，DDC 的應變門檻值會下降至 7%左右，但僅出現零星的微裂紋。

針對不同環境的運用要求，不同材料內的合金種類差異極大，難以預測材料的銲接性，因此建議材料性質模擬及 Gleeble 模擬試驗等能力建立，以期降低本所研發所需經費及人力，加速本所相關研發計畫的執行。3D 列印為近來受人重視的技術之一，其特性與本所的覆銲技術類似，應可評估轉變相關覆銲技術於 3D 列印的可行性。

銲接工程包含材料冶金、應力計算分析、自動控制及非破壞檢測等工作，未來計畫應整合相關工作項目，並與國內廠家密切合作，共同進行銲接技術研發計畫，符合國內產業需求，以便獲得最大的研發成果效益。

目次

一、目的

此行為前往美國俄亥俄州立大學材料科學與工程學系的銲接學程(welding program)實習 Strain to Fracture (STF)實驗並評估鎳基合金銲道的失延裂紋(Ductility Dip Cracking, DDC)敏感性。

二、過程

104 年 06 月 18 日~06 月 19 日　往程（台北－美國 紐約－美國 俄亥俄州哥倫布市）

06 月 20 日~09 月 25 日　核能組件銲接修補技術實習

09 月 26 日~09 月 28 日　返程 （美國 俄亥俄州哥倫布市－美國 紐約－台北）

三、核能組件銲接修補技術實習

(一)實習機構介紹

本次實習機構為美國俄亥俄州立大學材料系銲接學程(welding program)。俄亥俄州立大學為美國著名的研究型大學之一，共有哥倫布市(主校區)、萊馬、曼斯菲爾德、馬里恩、紐華克和渥斯特的校區，其材料系銲接學程(welding program)位於哥倫布市。該學程前身為俄亥俄州立大學銲接工程系，後來因為資源整合，而整併為材料系的一部份。該學程除與校內數個研究中心合作外，該學程與 Edison Welding Institute 同在一棟建築物內，彼此間共享研究資源。

(二)Strain to Fracture Test (STF Test)

一般而言，金屬延性隨溫度升高而增加，但有些金屬在靠近固相點附近會有延性下降的現象，因這延性下降的趨勢又深又窄，故稱此延性下降的現象為 Ductility Dip，如圖 3 所示。銲接過程中，當此試片的應變大於延性時，即發生失延裂紋(Ductility Dip Cracking, DDC)。

目前此種銲接性測試主要藉由 STF 及 Varestraint Test 等兩種試驗。材料在不同溫度及不同應變的 DDC 敏感性可由 STF 試驗獲得，以便決定 DDC 發生時的溫度及應變門檻值(Threshold)，可以相對進行定量化測試；而 Varestraint Test 則無法進行不同溫度的 DDC 敏感性試驗。

圖 5 為本次實習工作執行流程的示意圖。其中，試片銲接及切割等準備工作

在台灣執行，試驗所用的銲材與母材成份如表 1 所示。圖 6 為銲道示意圖，依 STF 試片尺寸(如圖 7 所示)要求，完成試片切割完成後，寄往美國實習單位，由台灣實習人員進行後續製備工作及實驗。

在美國實習單位時，以氬銲機進行銲點準備，確保觀察區域內的組織一致。在執行點銲時，先將試片放入銅夾具內，以利試片於點銲後散熱，如圖 8(a)所示。點銲完成後，將試片上的銲點處研磨平坦(至#800 砂紙)，如圖 8(d)所示，以利完成 STF 試驗後觀察。

除銲點準備外，STF 試片還需要標記應變量測點及銲接熱電偶。因為 Gleeble 試驗機無法精確控制應變量，需藉由外部參考點的位移變化，確認試片的應變量。此外，Gleeble 試驗機需以外部熱電偶為參考溫度，控制加熱速度，圖 9 為熱電偶銲接中及完成後照片 。

文獻結果[3,4]顯示，此系列合金最容易在 950℃發生失延裂紋(DDC)。在有限的試片下，選擇 STF 的測試溫度為 950℃，依不同應變設定，進行不同長度拉伸。完成測試後，先量測應變參考點的距離，藉此評估應變變化。之後，在立體顯微鏡下，計數各試片的 DDC 數目，並繪製成 STF 的測試結果，如圖 10 所示。

測試結果顯示，308L 銲道受約 9.8%的應變時，開始出現 DDC 裂紋，之後隨應變量增加而急遽上升；307Si 與 347 開始出現 DDC 的應變值各約為 11.1%及 13.3%，316L 出現 DDC 的應變值約在 7.0%左右，但裂紋數未隨著應變量而顯著增加。

(三)SSDTA 與 Cast Pin Tear Test

在實習過程中，參觀該學程的 SS-DTA 量測材料相變化溫度、Cast Pin Tear Test 及 Varstrain Test 等測試設備。相關設備相對簡易，值得本所作為技術發展參考。圖 11 為 SS-DTA 設備及 CCPT 設備示意圖。

(四)材料模擬軟體

銲接過程中，升溫及降溫將影響銲件的應力變化及變形，因此，兩者亦為銲接研究中的重要討論事項。該單位以 Abaqus 為主要的力學模擬軟體，用以評估銲接後的熱應力及變形分佈。此外，該單位亦設置 Sysweld 的專門銲接模擬軟體，供學生使用。

除力學模擬外，JMatPro 及 Thermal Cal.等兩種材料性質模擬軟體亦被採用於該單位中，兩種軟體都可以用於合金設計及銲接過程的材料性質變化模擬。

四、心得

銲接的運用極為廣泛，該學程的研究題目包含石化、汽車、核能等產業，內容除銲接製程開發、新銲接製程評估、材料相變化研究、機械性能改善與耐蝕性能評估。此外，非破壞檢查與銲接兩者緊密連結，提供銲接產業所需的技術與服務。

因此，銲接的研究領域非僅侷限在材料性質的變化，對於現場實務而言，銲接製程中的力學變化、銲接執行的設備控制及銲接後的非破壞檢驗已是銲接工程中的重要工作項目。本所除對材料性質及非破壞檢驗有較深入的研究外，其他項目仍待努力。

軟體模擬的使用有利於縮短銲接技術發展的時程，並降低所需的成本，目前本所僅著重於銲後的應力及變形，仍無材料冶金性質模擬能量。對銲接計劃來說，異材銲道的成份混合區容易產生相變化，進而引發缺陷產生，若有相關軟體輔助，應可預測有害相形成並加以防治，避免銲接缺陷產生，加速研究計畫執行。建議應逐步建置相關軟體並培養人才，以便加速本所計畫研發。

就材料性質模擬而言，目前有 JMatPro 及 Thermal Cal.等兩種材料模擬軟體。Thermal Cal.有較多的文獻使用紀錄，該軟體已被運用於合金發展的研究，但國內目前仍無相關運用紀錄。對 JMatPro 的模擬軟體來說，使用介面簡單且容易上手，已有國內代理商並有數個相關單位採用；惟該軟體為封閉性軟體，無法自行修訂資料庫，因此使用侷限度較大。

Gleeble 試驗機為銲接研究中的重要工具，該設備不僅可用於金屬高溫性質測試，亦可進行銲接製程模擬及試片製備之用，為該單位的重要研究設備。目前國內僅中鋼公司及工研院南分院有相關設備，但中鋼公司的設備不易商借，工材所的設備則為舊型且其儀器可用度仍待確認。

本所若欲從事高溫金屬研究，應透過與該單位合作或其他模式，規劃設備使用的研究計畫，逐步累積該設備的使用經驗，評估建置 Gleeble 試驗設備的可行性及推展後續研發工作。

在實習過程中，該學程自行組裝 SS-DTA、Cast Pin Tear Test 及 Varstrain Test 等測試設備，量測材料在冷卻過程的相變化溫度、定量評估材料凝固熱裂及材料銲接熱裂。依計畫需求組裝相關設備或調整設備使用機能，因此所內應該建實驗設備的自動化控制能力，以便自行開發研究設備，同時增加設備零件的通用性及使用率，以利可加速研發進度。

除此之外，美國的銲接人力短缺，急需補充銲接新血。針對相關的人員訓練，已有數個銲接廠商發展出虛擬模擬設備，學員可透過該設備進行銲接模擬，進而修正自己的銲接姿態，以避免銲接缺陷產生。除此之外，機器人及機器手臂也逐漸運用於銲接產業中，有別於以往用於汽車產業的電阻銲接，已有許多整合 TIG 跟 MIG 的市售銲接設備，用於固定銲道的銲接，增進銲接品質。本所也應評估機器手臂的銲接製程，因應未來產業發展的需求。

除鎳基合金葉片修補外，一般人認為銲接產業屬於比較粗重的工作，產業技術等級不高。實習過程中發現，該學程也發展 3D 列印技術，使用金屬粉末為製程材料，用於鎳基合金葉片製作。本所建立的的覆銲技術為堆銲型態的銲接，只要改變銲接製程技術及銲接過程的控制方式，應該可以達到 3D 列印的要求。在考量本所銲接技術的轉型需求上，應可將 3D 列印的列為未來技術發展的方向。

五、建議事項

(一) 持續派員前往國外機構實習，吸收相關銲接修補技術資訊，以作為本所日後技術發展參考。

(二) 透過與該單位合作或其他模式，逐步規劃 Gleeble 設備使用的銲接研究計畫，累積相關使用經驗，以利本所後續研發工作推展。

(三) 逐步建置材料冶金性質模擬能力，以便加速本所相關計畫研發。

(四) 與國內廠家密切合作，共同進行銲接技術研發計畫，以符合國內產業需求。

參考文獻

[1] John C. Lippold, Welding Metallurgy and Weldability, Wiley & Sons, Inc., New Jersey, 2015.

[2] Nathan E. Nissley, Intermediate Temperature Grain Boundary Embrittlement in Nickel-base Weld Metals, Ph.D. Dissertation, The Ohio State University, Columbus, OH, 2006.

[3] http://wjmg-mse.org.ohio-state.edu/cpttImprovement.php.

[4] S. Kiser, R. Zhang and B. Banker," A New Material for Improved Resistance to Ductility Dip Cracking," Trends in Welding Research 2008: Proceedings of the 8th International Conference, June 1-6, 2008, Pine Mountain, Georgia.

[5] N.E. Nissley, J.C. Lippold, Ductility-Dip Cracking Susceptibility of Nickel-Based Weld Metals: Part 2 — Microstructural Characterization, Welding Journal (2009), Vol. 88, pp.131s-140s.

Table 1 the compositions of the base metal and the weld metals (wt. %)

	C	Si	Mn	P	S	Cr	Ni	Mo	Cu	Nb+Ta	Fe	Ti	Remark
CF8A	0.063	1.43	0.76	0.034	0.039	20.6	8.67	0.03	-	-	Bal.	0.01	Plate
308L	0.02	0.51	1.94	0.01	0.003	20.3	10.3	0.09	0.09	-	Bal.	0.002	wire
307Si	-	1.93	6.11	0.049	-	18.41	8.18	0.07	0.16	-	Bal.	0.001	wire
347	0.043	0.44	1.78	0.024	0.009	19.5	9.1	0.23	0.12	0.64	Bal.	-	wire
Alloy 52MSS	0.023	0.11	0.31	0.004	0.0005	29.49	52.36.	3.51	0.05	2.51	11.45	0.18	wire

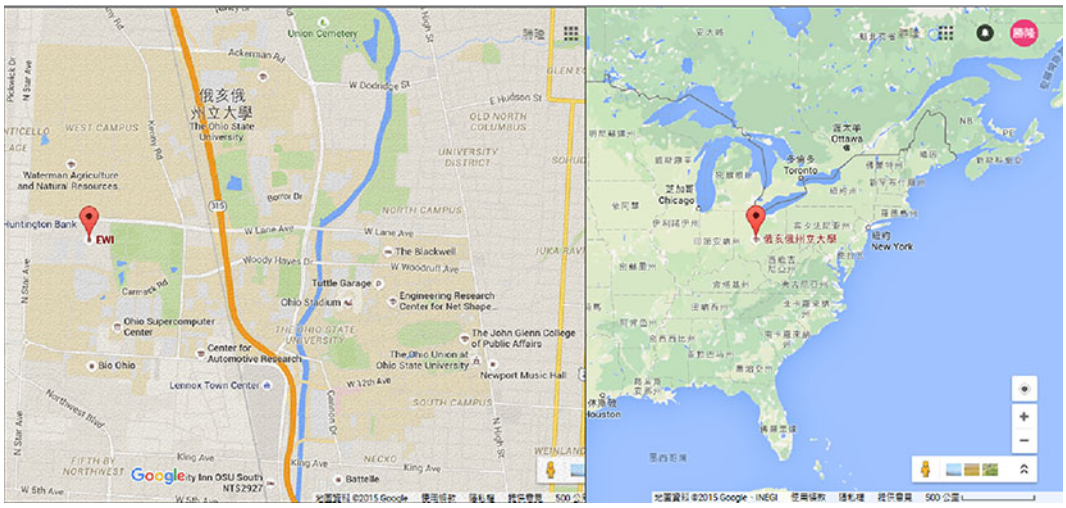

圖 1 俄亥俄州立大學材料系銲接學程(welding program)地圖上位置。

圖 2 俄亥俄州立大學材料系銲接學程館舍。

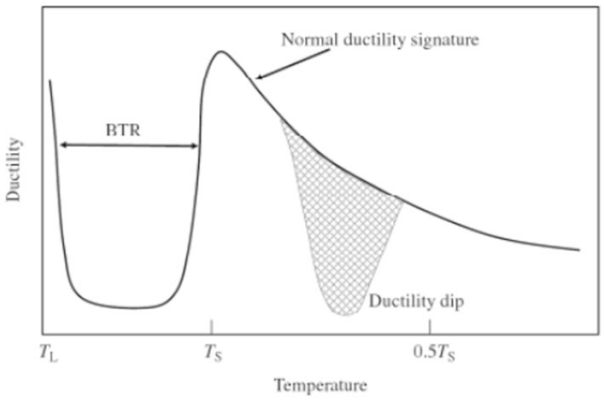

圖 3 有失延現象材料的延性隨溫度變化示意圖[1]。

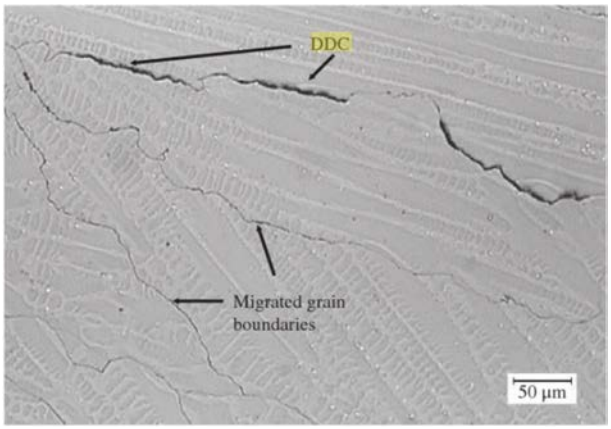

圖 4 鎳基合金銲道內的 DDC 與遷移晶界(Migrated grain boundaries)[1].

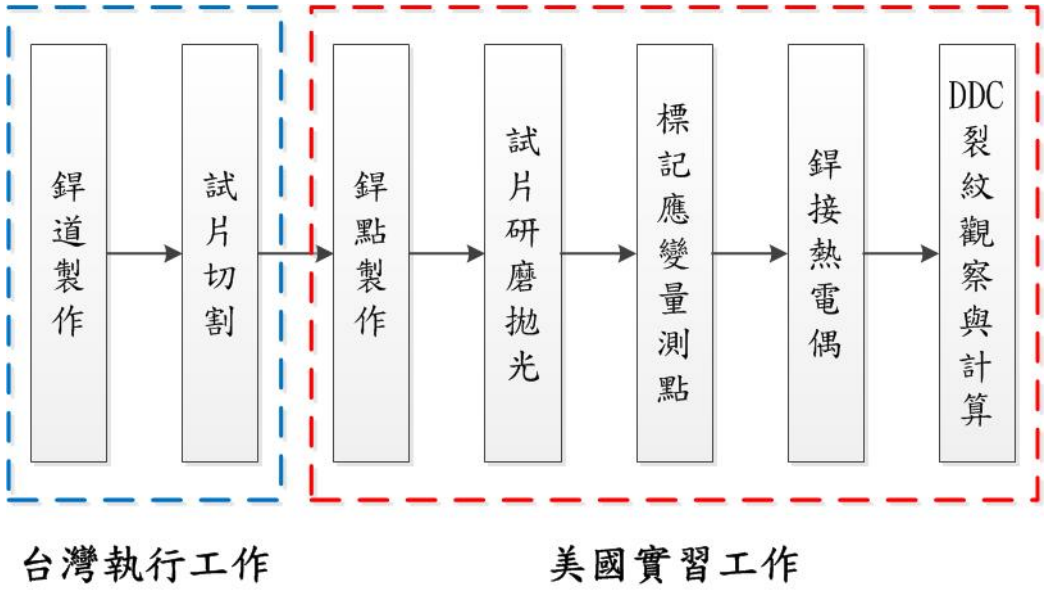

圖 5 實習工作執行流程示意圖。

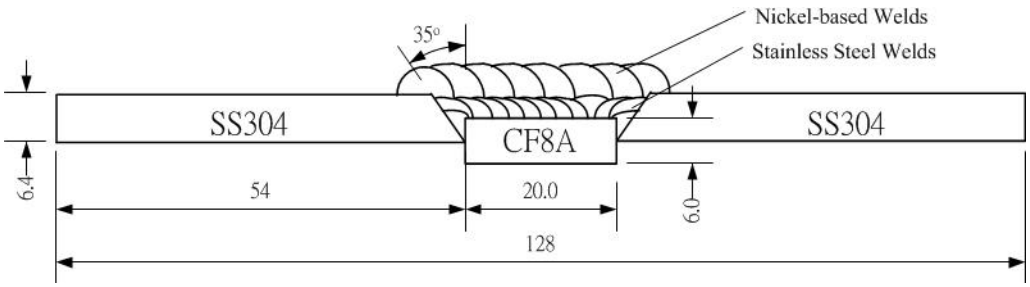

圖 6 銲道試件製作示意圖。

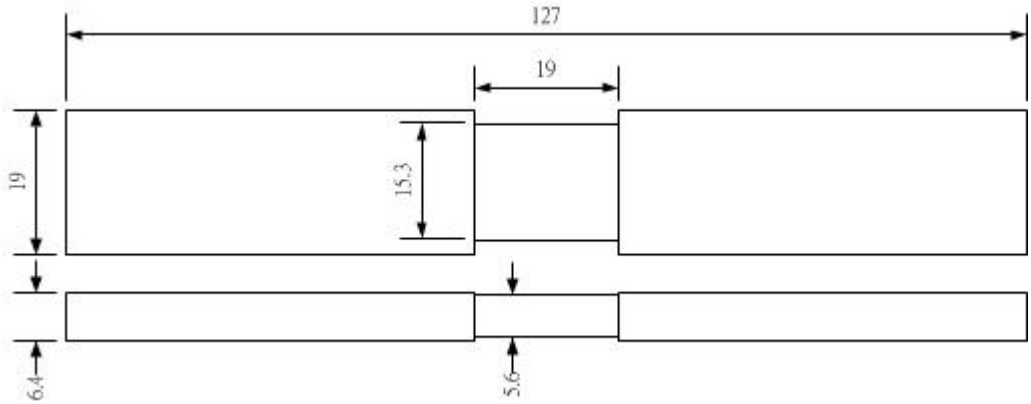

圖 7 STF 試片尺寸示意圖。

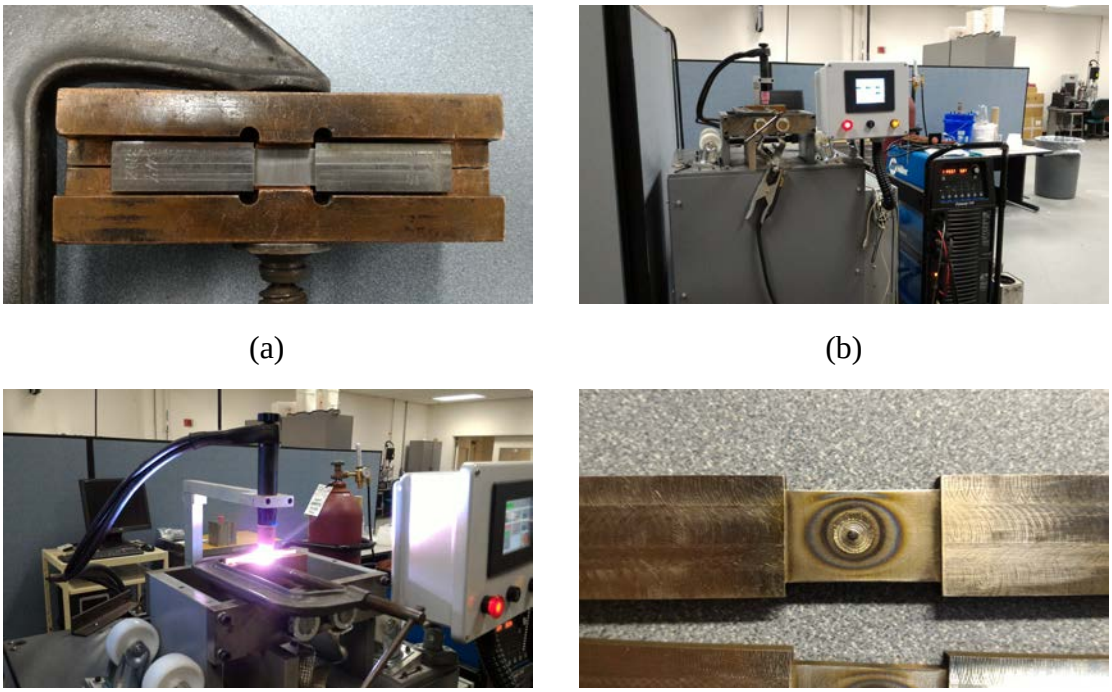

(a) (b)

(c) (d)

圖 8 STF 試片進行點銲準備:(a)將試片放如銅夾具內；(b)試片及夾具放置於接台上；(c)進行銲接；(d)點銲完成的試片形貌。

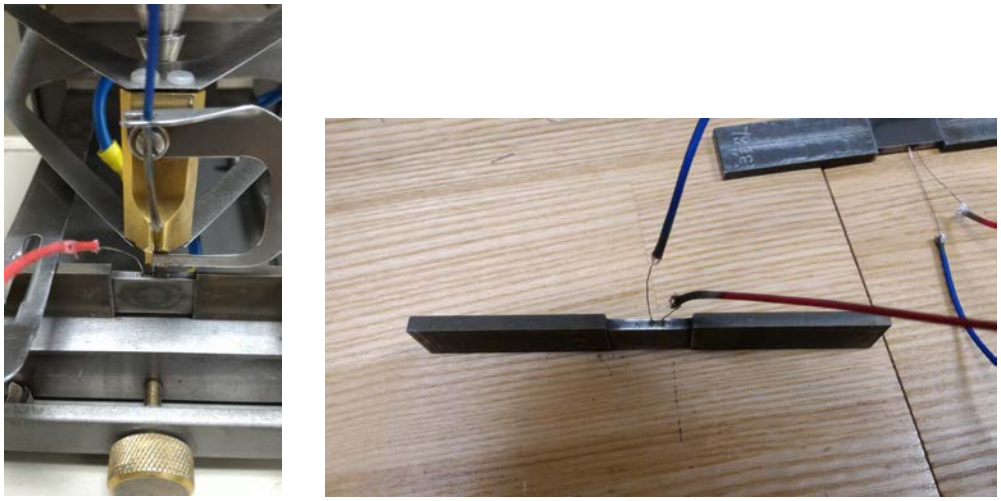

圖 9 試片點銲熱電偶:(a)進行熱電偶銲接; (b)熱電偶銲接完成後的試片形貌。

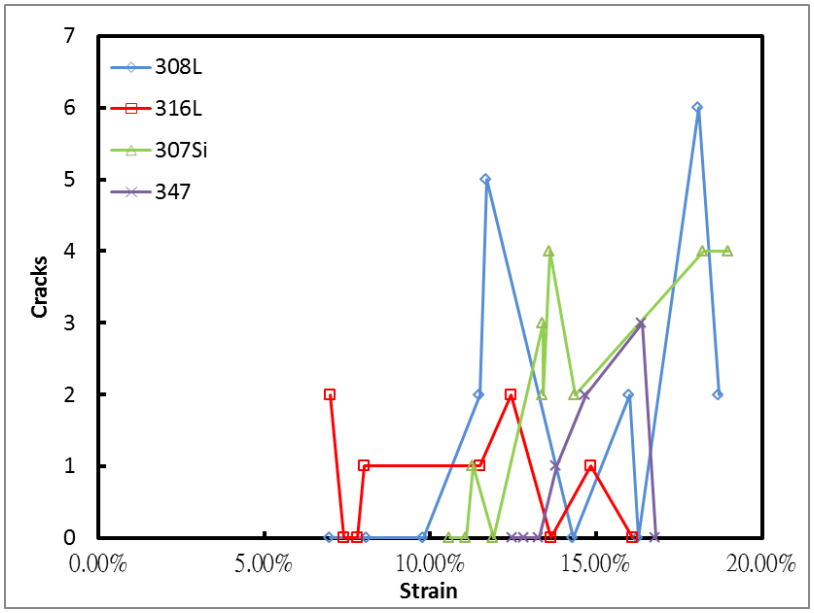

圖 10 STF 測試結果。

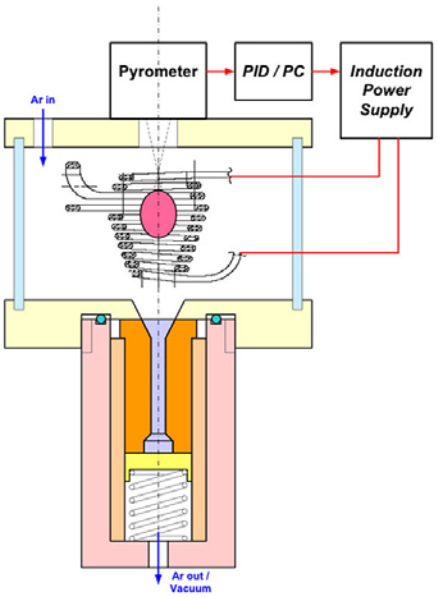

(a) (b)

圖 11 SSDTA 與 CCPT 設備照片與示意圖: (a) SSDTA 設備照片；(b)CCPT 測試設備示意圖[3]。

附件 **1**

S. Kiser, R. Zhang and B. Banker," A New Material for Improved Resistance to Ductility Dip Cracking," Trends in Welding Research 2008: Proceedings of the 8th International Conference, June 1-6, 2008, Pine Mountain, Georgia.

A New Welding Material for Improved resistance to Ductility Dip Cracking

S.D. Kiser, R. Zhang
Special Metals Welding Products Company, Newton, North Carolina, USA

B. A. Baker
Special Metals Corporation, Huntington, West Virginia, USA

Abstract

Nickel-Chromium-Iron alloys and welding products have been used throughout the life of the nuclear welding industry. From the beginning, Welding Electrode 182 and Filler Metal 82 were used to weld alloy 600 until they were found to be susceptible to primary water stress-corrosion-cracking (PWSCC). This brought about the need for a 30% Cr-containing alloy 690 along with Welding Electrode 152 and Filler Metal 52. These materials were resistant to PWSCC, but the welding products were found to be susceptible to ductility dip cracking (DDC). Because DDC is a solid state cracking phenomenon that may occur in highly restrained austenitic welds, most of the existing tests were ineffective for measuring DDC. The Ohio State University welding group introduced the Strain-to-Fracture (STF) test to measure the tendency for DDC. A number of nuclear welding materials have been subjected to STF testing and a new nickel alloy material with 30% chromium, INCONEL® FM52MSS, has shown substantially improved DDC cracking resistance when measured with the STF test. This paper discusses the development and performance of the welding material and the results of STF test of this new alloy.

Introduction

From the initiation of the commercial nuclear power generation industry, INCONEL® alloy 600 and INCONEL® Welding Electrode 182 (ENiCrFe-3) and Filler Metal 82 (ERNiCr-3) were chosen to resist the corrosion environment in nuclear reactors and steam generating equipment. After several years of worldwide operating experience, these materials were found to be susceptible to primary water stress corrosion cracking (PWSCC) due to their insufficient chromium contents [1-4]. Therefore, the alloy 600 and welding materials 182 and 82 have largely been replaced with 30% chromium-containing materials known as INCONEL® alloy 690 and INCONEL® Filler Metal 52 and Welding Electrode 152 in USA and other countries. These materials have been shown to be free from (PWSCC) cracking in operating reactors for over 15 years [1].

However, fabricators have found and identified a phenomenon known as ductility-dip cracking (DDC) that may occur during weld fabrication which has been found to be associated with austenitic materials of several types such as nickel-base, Ni-Cu alloys, Cu alloys, and stainless steels. Early ductility-dip cracking (DDC) that formed in weld metals was usually small, and was often referred to as a 'micro-fissuring'. Although this type of cracking (DDC) was identified as early as 1961 by Rhines and Wray [5], this term micro-fissuring was indiscriminately applied to both solidification cracking and to DDC until the early 1990's.

DDC is a solid-state, elevated temperature phenomenon that has been observed in thick-section, multipass austenitic stainless steel and nickel-based alloy weld metals characterized by large grain size and high restraint. An example is shown in Figure 1. The mechanism has been postulated to be the result of "ductility exhaustion" shown in Figure 2 along the grain boundary with grain boundary sliding and the relative orientation of a grain boundary to an applied strain increasing susceptibility to DDC. Although the occurrence of DDC is sometimes unnoticed, in applications where there is low defect tolerance, such as nuclear fabrication, its minimization is highly desirable.

INCONEL® Filler Metal 52M (ERNiCrFe-7A) has reported the improvements of DDC resistance over INCONEL® Filler Metal 52, however, the applications involving overlays (PWOL, SWOL, etc.) are insufficiently demanding to highlight the severity of cracking that can occur with higher restraints and heavier section welds[6]. In fact, the advent of much improved weld bead cleanliness presented by 52MS had a greater impact on product acceptance than improvements in DDC resistance. Recently a new generation welding material of the 52 family, INCONEL® Filler Metal 52MSS, was invented and patented by Special Metals Welding Products

Company and AREVA. This new alloy contains about 2.5 wt.% Nb and 4.0 wt.% Mo, which have been shown to improve DCC resistance dramatically. This paper will present the substantially improved DDC resistance of this alloy and the function of Nb and Mo on DDC resistance.

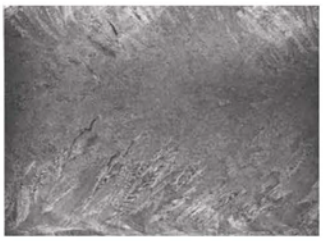

Figure 1, Ductility dip cracking (DDC) of trailing, solidified portion of linear varestraint test.

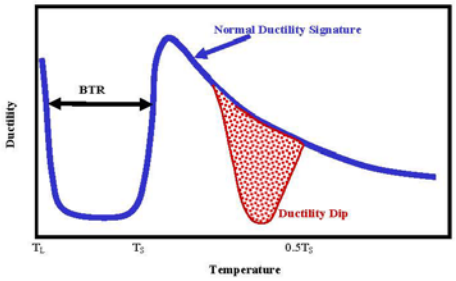

Figure 2. Schematic that represents the mechanism of ductility-dip cracking.

Materials and Sample Preparation

Six high-Cr weld metals (denoted as 3W-1, 3W-2, 3W-3, 3W-4, 52MSS (1), and (2)) with varying contents of Nb and Mo were used in this study. The chemical compositions of these alloys are presented in Table 1. Usually INCONEL® Filler metal 52MSS contains ~30% Cr, ~2.5% Nb and ~4.0% Mo and other elements. Other different types of Ni-base filler metals are given in Table 1 for comparison.

Multipass butt joint plates were made by the automated gas tungsten arc welding (GTAW) and gas metal arc welding (GMAW) processes. The base metal used for these joints was alloy 690. Dog bone-like samples, as shown in Figure 3, were sectioned transversely from the slotted butt joint plates and ground to the final dimension. Then, a GTAW spot weld was made at the middle of the pre-deposited weld on both sides, as presented in Figure 3. The circular geometry of this spot gives a radial distribution of grain boundaries so that cracking resulting from the axial strain during the STF test will occur along the most susceptibly oriented grain boundaries. Complete details of the STF test are given in Reference 7.

The tested samples were then evaluated for cracks using a stereo microscope up to 30X magnification. The degree of DDC in a given sample is determined by counting the number of cracks in the elongated spot weld of both sides of the sample, then dividing by two. Only cracks that were distinguishable at up to 30X magnification were included in the count. Subsequently, the STF tested samples were prepared for metallographic observation by grinding, polishing and then electrolytic etching in a 10% chromic acid solution at 1.5-2V for 30 s. Scanning electron microscopy (SEM) and EDS analysis was performed on a Sirion SEM/FEG and Phillips XL-30 ESEM/FEG at 15kV.

Table 1. Chemical compositions of different nickel base filler metals (wt.%)

Element	FM82	FM52	FM52M	3W-2	3W-3	3W-4	3W-1	52MSS (1)	52MSS (2)	68HP	69HP
C	0.031	0.026	0.02	0.026	0.019	0.012	0.02	0.026	0.024	0.029	0.005
Mn	2.97	0.24	0.80	0.05	0.97	2.64	0.18	0.19	0.79	0.90	1.21
Ni	72.34	58.82	59.54	56.62	59.73	58.31	61.79	54.67	53.46	58.81	57.0
Cr	20.57	28.91	30.06	29.0	29.24	26.8	29.11	29.92	30.34	29.94	30.0
Fe	0.95	10.53	8.22	8.35	6.30	9.04	3.24	8.31	8.18	8.80	9.15
Nb	2.5	0.03	0.83	2.46	2.11	2.53	2.19	2.57	2.49	<0.01	1.83
Mo	-	0.04	0.01	1.87	0.75	<0.01	3.04	3.83	4.01	<0.01	<0.01
S	0.002	<0.001	0.001	<0.001	0.001	0.012	0.001	0.0013	0.0014	0.001	0.001
P	0.004	0.004	0.003	<0.003	<0.003	0.006	0.001	0.0001	0.009	<0.003	0.004
Ti	0.32	0.55	0.224	0.34	0.32	0.13	0.231	0.193	0.188	0.68	0.39
Al	-	0.66	0.11	0.24	0.22	0.10	0.069	0.07	0.218	0.75	0.20
Si	0.16	0.15	0.09	0.08	0.08	0.39	0.115	0.119	0.21	0.13	0.11
Cu	0.01	0.02	0.02	0.06	0.04	0.01	0.013	0.059	0.06	<0.01	<0.01
Mo+Nb	2.5	0.07	0.84	4.33	2.86	2.53	5.23	6.4	6.5	<0.02	1.83

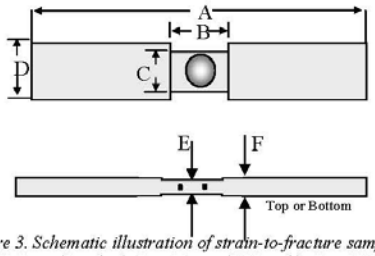

Figure 3. Schematic illustration of strain-to-fracture sample. A = 12.7 cm (5 inches), B = 19 mm (0.75 inch), C = 15.3 mm (0.6 inch), D = 19 mm (0.75 inch), E = Nominally 5.6 mm (0.22 inch), F = 6.4 mm (0.25 inch).

Results and Discussions

STF test results for filler metal 52MSS are presented in Figure 4. The numbers in parenthesis represent the number of cracks found on both sides of the sample divided by two. The black numbers represent the DDC results of an early experimental heat 52MSS then identified as 52X-H. The black solid line represents the approximate threshold strain for cracking for the initial experimental heat of 52MSS.

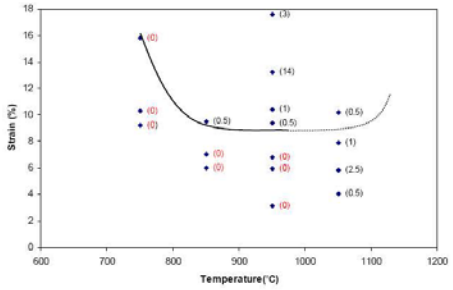

Figure 4. Initial STF results for Filler Metal 52MSS (then called 52X-H).

The STF results for Filler Metal 52MSS are compared to the STF data published for Filler Metal 52 and Filler Metal 82, as shown in Figure 5[6-7]. The results indicate that the DDC resistance of the initial heat of Filler Metal 52MSS is much better than Filler Metal 52, another 30% Cr nickel-base alloy, and even superior to Filler metal 82, which is known to be moderately resistant to DDC under high-restraint welding condition. Because the most susceptible temperature for DDC to occur in 30% Cr Nickel-base welding alloys is 950˚C, preliminary screening is often performed at this temperature.

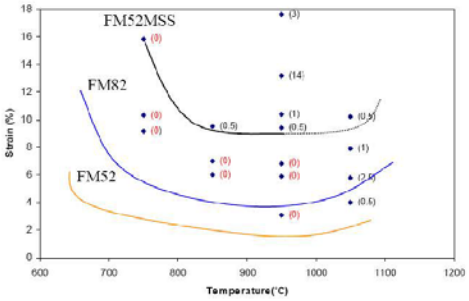

Figure 5. Comparison of the Filler Metal 52MSS threshold strain for cracking to the STF results of Filler Metal 52 and 82.

A comparison of the STF results of different welding filler metals tested at 950˚C is provided in Figure 6. The horizontal bar in the column above each filler metal represents the threshold strain for cracking for that material while the numbers present the number of cracks that were present in the sample as a function of the strain. The temperature of 950˚C was selected for STF screening testing due to the maximum ductility-dip at this temperature illustrated in Fig. 2. In addition, experience has indicated that the cracking response at 950˚C correlates well with actual fabrication behavior and provides the most discerning data.

The STF results of three different heats of FM52M and three different heats of FM52MSS were shown in the Fig 6. FM52M-1 is an old heat sample tested two years ago. But recently two 52M samples (FM52M-2 and FM52M-3) after tightly controlling the minor elements and applying a special clean procedure show very good DDC resistance, FM52M-2 is close to FM82 performance while FM52M-3 is superior to FM 82. The threshold strain for cracking for FM52MSS is between 8-16% at 950˚C. These data are generated from testing 52X-H, FM52MSS-1, and FM52MSS-2 shown in Table 1 which contain 52MSS prescribed amounts of Nb and Mo. There are no cracks for the FM52MSS-1 sample at an applied strain of 15%, and no cracks for the FM52MSS-2 sample at an applied strain of 16%. No STF tests were done beyond these strains.

The data presented in the Fig. 7 provides the trend of the threshold strain for cracking with the content of Nb and Mo in experimental welds. It is clear that with increasing amounts of Mo in the filler metal when Nb is between 2% and 3%, the threshold strain for cracking increases. It is indicated that the 52MSS family containing 5-6.5% Nb+Mo when %Nb is at least 2%, exhibit the highest threshold strains and the best resistance to DDC cracking.

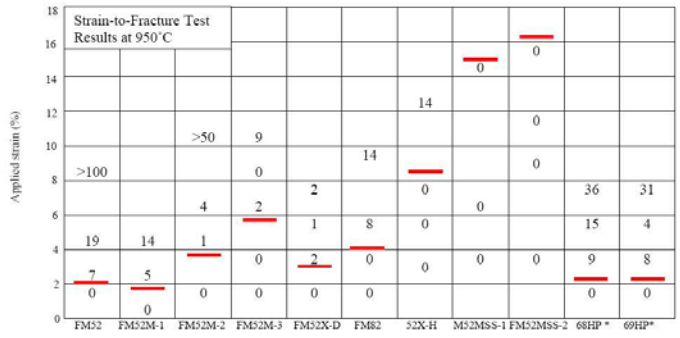

Figure 6. Strain-to-fracture test results for different nickel-base weld metals tested at 950°C. Some data from reference 7.

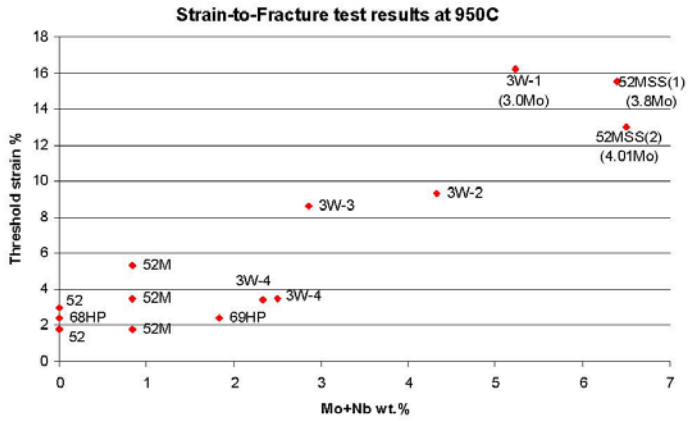

Figure 7. The relationship between threshold strain for cracking and the content of Ni and Mo. The STF results tested at 950°C. Note that alloy 3W-4 and data points to the left contain no Mo while 3W-3 and alloys to the right have Mo additions and show much improved STF performance.

In order to investigate the influence of Nb and Mo on the DDC resistance, microstructural examination of FM52M and FM52MSS was conducted by OSU researchers after STF testing. FM52M contains approximately 0.8% Nb and no Mo, boundaries are extremely serpentine. The straight grain boundaries of FM52M were populated with small, Cr-rich $M_{23}C_6$ carbides as shown in Fig 9. These carbides form in the solid-state as the weld metal cools to room temperature and were believed to have no effect on boundary pinning. The SEM image of FM52MSS weld metal shown in Fig. 10 indicates that the Nb-rich M(C,N) precipitates are spread while FM52MSS has a combined total of 6.5% Mo+Nb. Figure 8 show the patterns of migrated grain boundaries using electron backscattered diffraction (EBSD). It is clear that the FM52M boundaries are generally straight, while the 52MSS throughout the weld metal interdendritically instead of only in the grain boundaries. These well-distributed precipitates form at the end of solidification and are effective at pinning the migrating grain boundaries, resulting in serpentine grain boundaries that create interlocking grains. This structure is much more effective at resisting grain boundary sliding and thus greatly improves DDC resistance.

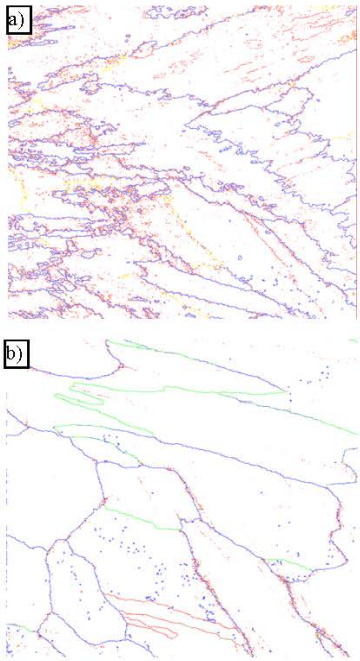

Figure 8. Electron backscattered diffraction (EBSD) patterns showing (a) serpentine migrated grain boundaries in FM52MSS and (b) the nearly straight grain boundaries of FM52M.

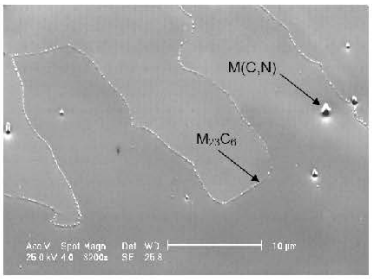

Figure 9. Undesirable long, straight grain boundaries with nearly continuous $M_{23}C_6$ carbides in FM 52M.

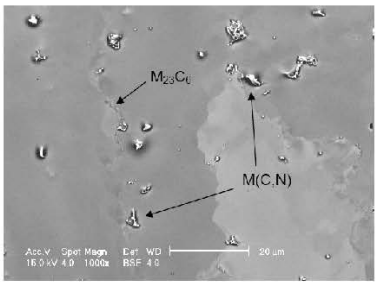

Figure 10. Backscattered electron SEM image showing visible M(C,N) precipitates and (Nb,Ni)-rich phases in the interdendritic regions and $M_{23}C_6$ carbides along a few of the grain boundaries. Noticeable grain boundary pinning by the large intragranular precipitates is still observed.

Summary

The current status of Nickel based alloys for nuclear construction is that 30% chromium-containing nickel-base alloys and welding products are necessary for primary water stress corrosion cracking (PWSCC) resistance. These materials have sufficient resistance to PWSCC, but the weld metals suffer from susceptibility to DDC cracking due to the tendency for long, straight grain boundaries during solidification and cool down. INCONEL® Filler Metal 52M provides reasonable resistance to DDC during fabrication and good resistance to PWSCC in nuclear service. But the newest 30% chromium-containing nickel alloy welding product, INCONEL® Filler Metal 52MSS, has been shown to provide outstanding DCC resistance and has been found in other research[8] to provide the same excellent PWSCC resistance as INCONEL® Filler Metal 52M.

Acknowledgments

The authors would like to acknowledge Dr. John Lippold from The Ohio State University for conducting STF testing and Dr. Nathan Nissley from ExonMobil Upstream research for SEM work. We also wish to thank these researchers for permission to use STF test results and illustrations. Also acknowledge Knolls Atomic Power Laboratory for PWSCC testing of FM52MSS.

References

1. J. Hickling and A. Ahluwalia, "Advanced Testing Techniques to Measure the PWSCC Resistance of Alloy 690 and its Weld Metals," Report 1011202, Electric Power Research Institute, Palo Alto, CA, USA, October 2004.
2. B. Miglin and G. Theus, "Stress Corrosion Cracking

of Alloy 600 and 690 in all Volatile Treated Water at Elevated Temperature," Report NP-5761M, Electric Power Research Institute, Palo Alto, CA, USA, 1998.
3. C. Amzallag, S.L. Hong, C. Pages and A. Gelpi, "Stress corrosion life assessment of alloy 600 PWR components," *Processings of Ninth International Symposium on Environmental Degradation of Materials in nuclear Power Systems-Water Reactors*, TMS, Warrendale, 1999, p.243.
4. S. kasahara, M. Sato, T. Ohya, M. Kanikawa and H. kanasaki, "Surface modification for PWSCC prevention of alloy 600 by a laser cladding technique," *Processings of Ninth International Symposium on Environmental Degradation of Materials in nuclear Power Systems-Water Reactors*, TMS, Warrendale, 1999, p.783.
5. F.N. Rhines and P.J. Wray, "Investigation of the Intermediate Temperature Ductility Minimum in Metals", *Transactions*, ASM, Vol 54, 1961, p 117-128.
6. J.C. Lippold and N.E. Nissley, "Further Investigations of Ductility-dip Cracking in High Chromium, Ni-base Filler Metals," presented at the IIW-IIC-326-06, Quebec City, Canada(August 2006).
7. N.E. Nissley and J.C. Lippold. "Development of the strain-to-fracture test for evaluating ductility-dip-cracking in austenitic alloys," *Welding Journal*, 82(12), 2003. P.355s-364s.
8. Unpublished Research by Dr. G.A. Young, Jr at Lockheed Martin Corporation (KAPL), Schenectady, NY 12301.

附件 2

Ductility-Dip Cracking Susceptibility of Nickel-Based Weld Metals: Part 2 — Microstructural Characterization

Ductility-dip cracking in Ni-Cr-Fe weld metals was attributed to grain boundary sliding in the temperature range from approximately 750° to 1150°C

N. E. NISSLEY AND J. C. LIPPOLD

ABSTRACT

Part 2 of the investigation of the ductility-dip cracking (DDC) susceptibility of Ni-Cr-Fe filler metals describes experiments and characterization designed to provide a better understanding of the DDC mechanism. The strain-to-fracture (STF) DDC susceptibility varied significantly with only minor changes in composition and was influenced by the solidification microstructure. Optical metallography, electron backscatter diffraction (EBSD), thermodynamic calculations, and heat treatments were used to better understand microstructural factors that influenced susceptibility to DDC.

The DDC cracking susceptibility was compared with thermodynamic calculations to better understand how carbide precipitation affects grain boundary sliding and the mechanism for DDC. Macroscopic grain boundary locking occurs in alloys that form interdendritic MC-type carbides at the end of solidification. A significant decrease in the DDC susceptibility was found in alloys with Mo and Nb additions that resulted in a dense distribution of skeletal MC-type carbides. The carbide morphology and distribution affects boundary migration and results in wavy or tortuous grain boundaries that mechanically lock the grain boundaries and oppose the sliding that promotes cracking. Microscopic grain boundary locking occurs in alloys that form intergranular $M_{23}C_6$ carbides. The distribution, morphology, and precipitation kinetics of these carbides affect their ability to limit grain boundary sliding.

Solutionizing and subsequent precipitation heat treatment improved the resistance to DDC. This resistance was attributed to microstructure homogenization, and $M_{23}C_6$ precipitation that resulted in reduced grain boundary sliding. In one Filler Metal 52M alloy, the elongated intergranular $M_{23}C_6$ carbides promoted dynamic recrystallization during STF testing that was attributed to particle stimulated nucleation (PSN).

Based on this investigation, DDC in Ni-Cr-Fe weld metals is clearly attributed to grain boundary sliding in the temperature range from approximately 750° to 1150°C. The precipitation of MC-type carbides at the end of solidification results in pinning of the migrated grain boundaries that make these boundaries "tortuous" and resistant to sliding. In addition, the precipitation of $M_{23}C_6$ carbides in the solid state provides additional microscopic locking of the boundaries that further improves resistance to DDC.

N. E. NISSLEY, formerly a graduate research associate at The Ohio State University, is currently with ExxonMobil Upstream Research Co., Houston, Tex. J. C. LIPPOLD is a professor in the Welding Engineering Program at The Ohio State University, Columbus, Ohio.

Introduction

In Part 1 of this investigation, the ductility-dip cracking (DDC) susceptibility of Ni-Cr-Fe filler metals was evaluated using the strain-to-fracture (STF) Gleeble-based testing technique (Ref. 1). Part 2 of this investigation focuses on the mechanism of DDC in these weld metals. Numerous mechanisms for DDC have been proposed for multiple alloy systems and include sulfur embrittlement (Refs. 2, 3), grain boundary sliding (Refs. 3–7), and $M_{23}C_6$ precipitation-induced cracking (Ref. 8). The lack of consensus on the mechanism for DDC is due to multiple contributing factors that add to the complexity of DDC in different alloy systems. This complexity limits the use of some testing techniques where there are too many uncontrolled variables and limited options for a systematic evaluation. The Gleeble-based STF test has demonstrated significant advantages for assessing DDC susceptibility, including 1) a reproducible starting microstructure, 2) a single testing temperature that isolates the DDC-susceptible temperature field, 3) control of strain at the test temperature, and 4) can be used for both on-heating and on-cooling tests (Refs. 5, 9).

Based on previous research, there is a lack of consensus on the effect of composition on DDC susceptibility. Dix and Savage reported that in Inconel® X-750, carbides appeared to inhibit grain boundary sliding, which improved the ductility, and they found no evidence of embrittlement due to carbide precipitation (Ref. 7). Rhines and Wray reported that grain boundary shearing in Monel® was the cause of the DDC, and boundary orientation was important (Ref. 10). Similarly, Ramirez and Lippold reported evidence of grain boundary sliding in FM-52 and 82 and proposed that it was caused by a creep-like mechanism associated with grain boundary sliding (Refs. 11, 12). Haddrill and Baker reported that in 25-Cr/20-Ni stainless steels, increased carbon reduced DDC susceptibility, and concluded that the cracking could not be caused by strain-induced precipitation (Ref. 13). Arata et al. reported that an increase in carbon reduced cracking in stainless steels

KEYWORDS

Ductility Dip Cracking
Nickel-Based Alloys
Precipitation Heat Treatment
Grain Boundary Sliding
Weld Process Simulation
Strain-to-Fracture Testing

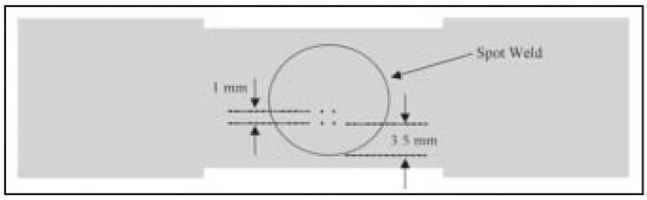

Fig. 1 — Schematic showing the location of the four indentions forming a 1- × 1-mm square inside the spot weld on the STF sample. The indentions were used to locate the same area for EBSD scans before and after STF testing and were located 3.5 mm from the edge of the spot weld. (Not to scale.)

Table 1 — All-Weld-Metal Compositions (wt-%) of the Three Experimental Alloys that Were Further Evaluated

	Mat. B (FM-52M)	Mat. C (FM-52M)	Mat. H (N/A)
Ni	59.54	60.38	53.87
Cr	30.06	29.5	30.18
Fe	8.22	8.04	8.2
Nb	0.83	0.82	2.48
C	0.02	0.03	0.021
Mn	0.80	0.77	0.8
Si	0.001	0.001	0.001
P	0.003	0.004	0.004
Si	0.09	0.12	0.2
Cu	0.02	0.01	—
Al	0.11	0.12	0.04
Ti	0.22	0.19	0.2
Mo	—	—	4
B	0.003	0.001	0.001
Zr	0.01	0.008	0.007

and attributed this to $M_{23}C_6$ carbides restricting grain boundary mobility. However, Young et al. tested a number of Ni-Cr weld metals and concluded that DDC was caused by $M_{23}C_6$ precipitation-induced cracking (Ref. 8). Zhang et al. reported that in Invar®, grain boundary sliding coupled with intergranular precipitates and serrated grain boundaries led to the observed DDC cracking (Ref. 14). Lin and Cola reported strain concentration at grain boundaries of FM-52 weld metal and proposed that the difference in ductility between the grain interiors and boundaries may account for the DDC cracking (Ref. 15).

Collins et al. found that additions of sulfur and/or hydrogen increased the susceptibility to DDC in FM-82 (Refs. 16, 17). Ramirez and Lippold reported that in FM-52 and 82 sulfur affected cracking but bulk sulfur levels were not sufficient to define DDC susceptibility (Ref. 11). Nishimoto et al. reported that in Alloy 690, sulfur and phosphorus had an embrittling effect on grain boundaries but reported a recovery with lanthanum additions (Refs. 3, 18, 19). Capobianco and Hanson proposed that for FM-52, the ductility-dip may be caused by the combined effect of sulfur embrittlement and local stress from $M_{23}C_6$ carbide precipitation (Ref. 20). Young et al. concluded that DDC in their Ni-Cr alloys was not controlled by grain boundary impurity segregation of sulfur (Ref. 8). In Invar, Matsuda et al. found that sulfur, oxygen, nitrogen, and aluminum promoted DDC while silicon and manganese inhibited DDC (Ref. 21). Nishimoto et al. found that the sulfur embrittlement of grain boundaries in Invar was accelerated by reheating during multipass welding (Ref. 2).

There have been numerous reports where Nb and/or Ti carbonitrides in Ni-based alloys have altered the grain boundary morphology and decreased the DDC susceptibility (Refs. 8, 11, 12, 22–28). This seems consistent with the extensive cracking observed in commercially pure nickel 200 reported in Part 1, which is essentially free of carbides (Ref. 1).

Several authors have reported that in Ni-based alloys the orientation of the boundary and the applied strain affected cracking (Refs. 12, 16, 23, 24, 26) and Kikel and Parker reported that rotating the weld 90 deg to the applied strain reduced DDC (Ref. 23). Davé et al. found that "special" grain boundaries in Alloy 690 were less susceptible to DDC than random boundaries (Ref. 29). Collins et al. observed that DDC only occurred along random, high-angle boundaries (Ref. 24).

Significant heat-to-heat variation continues to be reported, that, based upon our current understanding of the DDC mechanism, could not have been predicted solely by composition (Refs. 16, 25, 28). Additional understanding of the effect of bulk composition on ductility-dip cracking susceptibility is needed to understand and avoid cracking in the future.

Experimental Procedures

In Part 1, eight experimental Ni-Cr-Fe alloys were prepared and tested for DDC susceptibility with the STF test (Ref. 1). Based upon these results, materials B, C, and H (Table 1) were selected for further microstructural evaluation to better understand the factors affecting DDC susceptibility. Materials B and C are experimental Filler Metal 52M (FM-52M) alloys and material H is a FM-52M-like alloy with additions of 2.5% Nb and 4% Mo. FM-52M (AWS A5.14, ERNiCrFe-7A) is a second-generation welding wire for joining Alloy 690 in nuclear applications where SCC and DDC resistance are required.

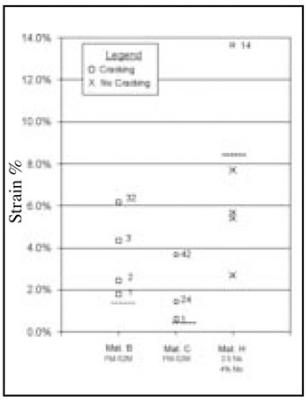

Fig. 2 — STF test results for baseline testing at 950°C for experimental FM-52M compositions. An "x" represents a tested sample with no DDC cracking and an "o" a sample with DDC cracking. The number next to the circle is the number of DDC cracks found in the sample. Materials B and C are experimental heats with the same target composition except for boron, and material H has higher Mo and Nb.

In the present work (Part 2), all of the alloys were evaluated before and after STF testing using optical microscopy, scanning electron microscopy (SEM), and electron backscattered diffraction (EBSD). The microstructural observations were compared with solidification and equilibrium thermodynamic calculations and with the STF testing results. Based upon these observations, samples were heat treated to alter the as-welded carbide distribution and then STF tested to better understand the effect of carbide precipitation on DDC susceptibility.

Microstructural Analysis

Samples prepared for optical and electron microscopy were mechanically polished through 3 µm diamond paste and then electropolished prior to each scan to expose a clean surface. Electropolishing was performed with a Struers LectroPol-5 using Struers A2 polishing solution and developed operating parameters (39 V, ~1.7 A/cm^2, 3 cm^2 mask, 18 flow, 22°C, 15

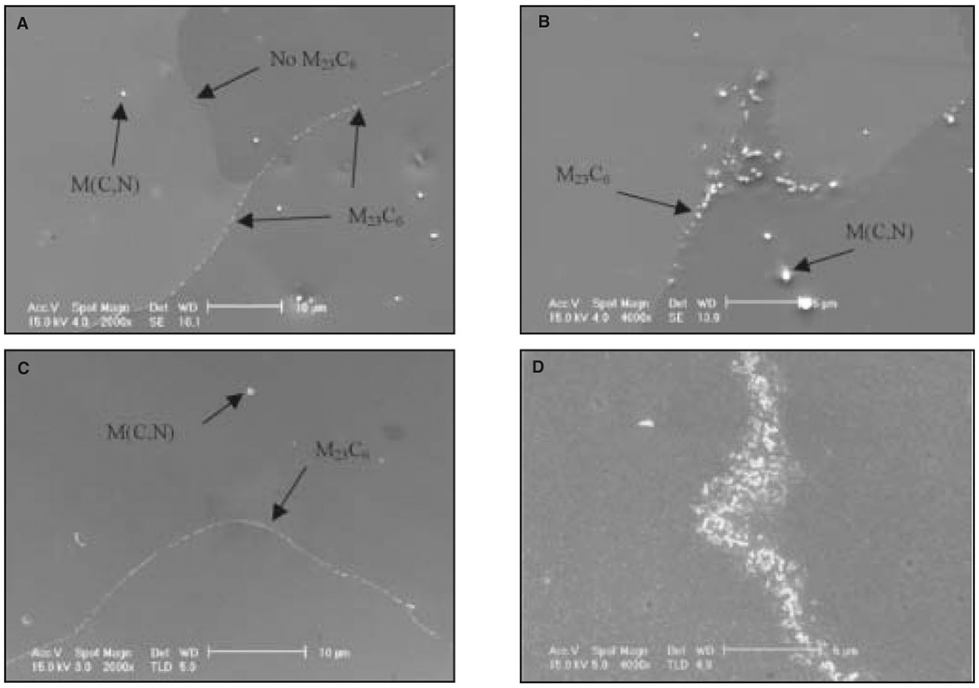

Fig. 3 — Material B sample showing the as-welded (spot weld) microstructure (A and B) and the STF tested (950°C) microstructure (C and D). M(C,N) carbides are visible in the interdendritic regions in both cases while the $M_{23}C_6$ carbides were found on select boundaries as welded and on almost all boundaries after STF testing.

s) (Ref. 5). Electropolishing was found to be beneficial as it produced a deformation-free sample surface required for EBSD but did not etch away the carbides, leaving them exposed above the surface. Samples were etched with a 10% chromic acid solution at 1.5 to 2 V for 30 s when required.

Strain-to-fracture testing was completed on-heating using standard testing procedures detailed in Part 1 (Ref. 1). On-cooling STF tests were not completed during this study due to the additional test variables that are introduced (e.g., peak temperature, cooling rate) and the fact that a significant number of cracks are observed in these alloys on-heating at low levels of strains. Standard STF spot welds with a 12.7-s downslope time were used for all reported data. Samples were heated in the Gleeble to the test temperature, held for 10 s, and strained different amounts. After cooling to room temperature, the strain and number of cracks were determined with the aid of a binocular microscope at magnifications up to 30 X. The results of the test are plotted on a temperature-strain plot with the number of cracks beside each point. The STF results include the threshold strain and the transition to gross cracking. The threshold strain is defined as the lowest strain over the entire DDC temperature range at which the material begins to crack. While the complete on-heating DDC temperature range was not tested for these alloys due to a limited number of samples, the use of the term threshold strain in this paper is used to describe the minimum strain at which the samples started cracking at 950°C. Other STF tests to date on FM-52 and FM-52M alloys (Refs. 9, 27, 30) have shown that 950°C can provide a reasonable estimate of the threshold strain for these alloys. The transition to "gross" cracking is defined as the strain where cracking becomes so abundant that cracks begin to grow and connect, making accurate crack counting difficult. The gross cracking transition can be defined when the slope of the number of cracks from one sample to the next exceeds approximately 10 cracks per percent strain.

Electron microscopy was performed with three separate scanning electron microscopes for imaging, EDS chemical analysis, and EBSD (Ref. 31). All SEM imaging and EDS analyses were performed at 15 keV, and EBSD was performed at 25 keV. Quantitative analysis of carbides with the EDS data was limited due to the size of the electron beam interaction volume. The EBSD data collection and analysis was performed with the EDAX TSL OIM™ software.

Deformation

Electron backscattered diffraction was performed before and after STF testing with a modified sample geometry. While the total STF sample length was reduced to 3.75 in. (9.5 cm) to accommodate the space limitations of the EBSD chamber, the gauge length and spot weld remained the same (Ref. 5). After the sample was prepared according to the standard polishing and etching procedure described previously, a set of four Vickers microhardness indentions were made on the sample surface with the use of a microme-

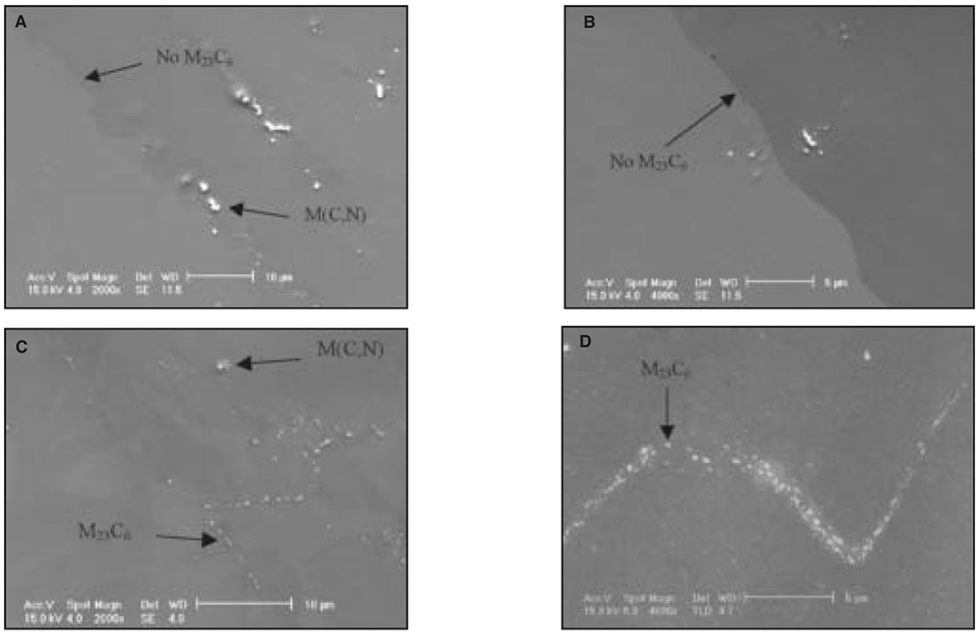

Fig. 4 — Material C sample showing the as-welded (spot weld) microstructure (A and B), and the STF tested (950°C) microstructure (C and D). M(C,N) carbides are visible in the interdendritic regions but no $M_{23}C_6$ carbides were found as welded and only sporadically after STF testing.

ter-controlled stage to form a 1-mm square inside the spot weld. The indentions allowed for the same location to be identified before and after STF testing on the sample in the tilted and polished condition that was required for EBSD — Fig. 1. The spot welds were typically 10 to 11 mm (0.41 to 0.45 in.) in diameter and the four indentions were located 3.5 mm (0.14 in.) from the edge to avoid the elongated columnar grains that formed near the edge of the spot weld and any abnormality that might exist in the center. The sample was then electropolished for 10 s to remove the etching effects, but leaving evidence of the Vickers indents and allowing for location identification for EBSD. Collected EBSD scans were 0.75-mm (0.3-in.) square with a 2-µm step size and centered inside the four microhardness indentions. Following the before-STF EBSD scan, the sample was STF tested, electropolished again for 10 s to remove the thin oxide layer, and then rescanned.

This technique provided information on how the microstructure accommodated the strain during the STF test and gave insight into what effect the starting microstructure had on DDC susceptibility. This technique was successful up to strains of approximately 4%. As the strain exceeded 5%, the amount of surface deformation was sufficient to prevent acquisi-

Table 2 — Results of Microstructural Analysis Compared with JMatPro-Ni v. 7 Thermodynamic Solidification Calculations* for Materials B, C, and H (Ref. 5)

	Material B		Material C		Material H	
	Spot Weld	STF	Spot Weld	STF	Spot Weld	STF
M(C, N)	0.5–2 µm Fig. 3A Predicted*	0.5–2 µm Fig. 3B	0.5–2 µm Fig. 4A Predicted*	0.5–2 µm Fig. 4B	1–5 µm Fig. 5A Predicted*	1–5 µm Fig. 5B
$M_{23}C_6$	Sporadic on GBs <0.5 µm	Consistent on GBs <0.5 µm	None Observed	Inconsistent on GBs <0.5 µm	None Observed	Sporadic on GBs <0.5 µm
Delta	N/A	N/A	N/A	N/A	Possible Predicted*	Possible
Laves	N/A	N/A	N/A	N/A	Possible Predicted*	Possible
Sigma	N/A	N/A	N/A	N/A	Possible Predicted*	Possible

*Note:"Predicted" indicates that the phase was present in the JMatPro calculations. "Possible" indicates that the EDS methods used were not sufficient to differentiate between the different phases.)

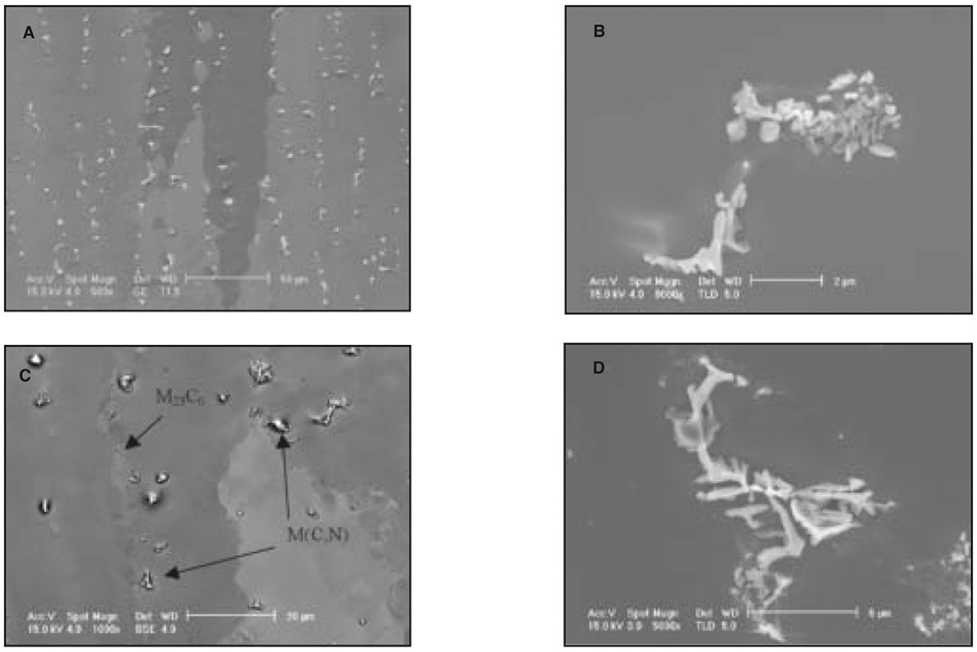

Fig. 5 — Material H sample showing the as-welded (spot weld) microstructure (A and B) and the STF tested (950°C) microstructure (C and D). Large M(C,N) carbides are visible in the interdendritic regions that resulted in wavy or tortuous grain boundaries.

tion of the EBSD diffraction pattern on heavily deformed portions of the sample.

Grain reference orientation deviation (GROD) plots were used to evaluate orientation differences within individual grains. The average orientation within a given grain was calculated and all points within the grain with the same orientation as the average were colored blue (0-deg deviation). As the angular deviation of the points increased from the average orientation, the color transitioned through green, yellow, orange, and red (16-deg deviation). The before and after GROD plots are insightful when evaluating how deformation is accommodated within a material. Additional information on the EBSD and GROD procedure can be found elsewhere (Ref. 5).

Carbide Engineering

JMatPro-Ni v. 7 by Thermotech Ltd. was used for all thermodynamic calculations. The nickel database included the following elements: Ni, Al, Co, Cr, Cu, Fe, Hf, Mn, Mo, Nb, Ru, Re, Si, Ta, Ti, V, W, Zr, B, C, N, and O. Any elements not listed in Table 1 were not used in the calculation except nitrogen, which was assumed to be 0.002 wt-%. Three primary types of calculations were performed: stable and metastable phases, solidification, and phase transformation (CCT/TTT) calculations (Ref. 5).

Sample heat treatment prior to STF testing was conducted with the Gleeble to alter the carbide type, size, distribution, and morphology. Samples were prepared using the same procedures used for STF testing but no mechanical force applied during heating. A solution annealing heat treatment at 1275°C for 1 min was used in conjunction with $M_{23}C_6$ carbide precipitation heat treatments at 700°C for 5 and 3.75 h for materials B and C, respectively. These temperatures and hold times were based upon thermodynamic calculations using JMatPro-Ni v. 7. The precipitation heat treatment temperature was selected to minimize grain growth while keeping the heat treatment times reasonable. Samples were heated to temperature at 100°C/s and afterward were allowed to free cool to room temperature without any external mechanical loading.

Results and Discussion

Based upon the STF results of Part 1 (Ref. 1), materials B, C, and H were selected for further evaluation to provide additional insight into the DDC mechanism. While both materials B and C had similar compositions (with the exception of a small difference in boron content), their DDC resistance varied significantly — Fig. 2. While both alloys cracked at relatively low threshold strains (< 1.5%), the additional strain required to transition to gross cracking varied significantly. Material B transitioned to gross cracking above 5% while material C transitioned around 1.5% strain. Material H was selected due to its high threshold strain (~8%) and general resistance to gross cracking (>14% strain).

Microstructural Analysis

Microstructural analysis was performed before and after STF testing on materials B, C, and H to better understand the effect of the microstructural evolution and carbide morphology on DDC suscep-

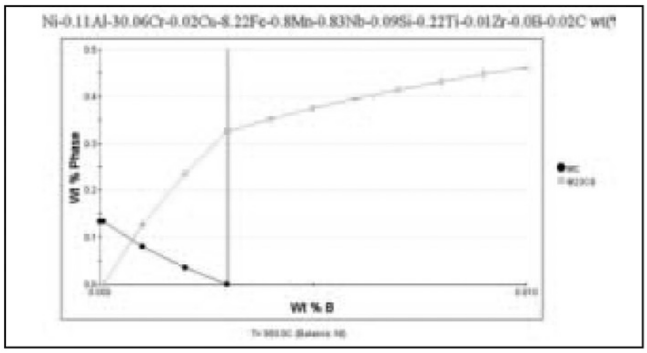

Fig. 6 — Effect of boron content (0 to 0.01 wt-%) on equilibrium carbide stability in material B at 950°C. The nominal boron composition of material B is marked as a vertical line at 0.003 wt-%.

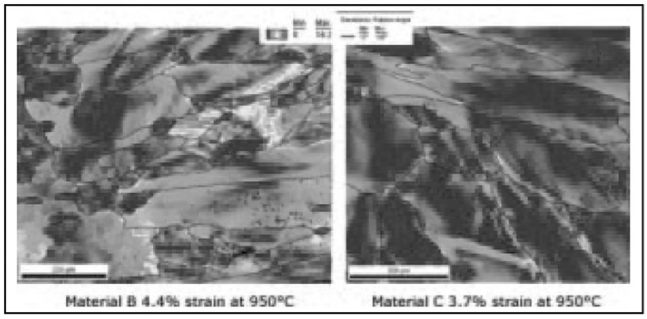

Fig. 7 — Grain reference orientation deviation plot of EBSD scan of materials B and C after STF test at 950°C. Blue indicates point with an orientation close to the average orientation of that particular grain while yellow and red indicate greater crystallographic deviation. The black lines represent high-angle (>10-deg) grain boundaries.

tibility. EDS was used for qualitative chemical analysis of the carbides in these alloys and those results were compared with the analysis of similar alloys completed previously (Ref. 26). The results of the carbide analysis from the microstructural characterization of materials B, C, and H are summarized in Table 2 along with the thermodynamic solidification and equilibrium JMatPro-Ni calculations (Ref. 5).

In the as-welded condition, electron microscopy of materials B and C revealed 0.5 to 1 μm Nb- and Ti-rich M(C,N) intragranular carbides that were sparsely dispersed through the microstructure. These intragranular carbides were not typically observed pinning grain boundaries as their size and distribution were inadequate to have a significant effect on the boundary migration at elevated temperatures — Figs. 3A and 4A. Cr-rich $M_{23}C_6$-type intergranular carbides were observed on the majority of grain boundaries in material B but the grain boundaries in material C were clean and practically free of carbides in the as-welded condition — Figs. 3B and 4B. In material B, the intergranular carbides were <0.5 μm in size and while carbides were observed on the majority of boundaries, the number of carbides varied from boundary to boundary and some of the boundaries remained free of carbides.

The as-welded microstructure of material H contained numerous larger 1- to 5-μm M(C,N) carbides that form along the solidification grain boundaries at the end of solidification and were found to be effective at pinning migrated grain boundaries — Fig. 5B. The morphology of some of the interdendritic carbides were difficult to characterize as the particles had a skeletal structure and were often composed of groups of smaller carbides agglomerated together (Ref. 5). JMatPro-Ni calculations of phase stability in material H included Delta, Laves, and Sigma phases, which were noted on Table 2 as "predicted." As these phases are Ni rich or Cr rich, they were difficult to distinguish from the gamma substrate with EDS and were therefore noted in Table 2 as "possible." Intergranular $M_{23}C_6$ carbides were not observed along the grain boundaries of material H in the as-welded condition.

The microstructures of materials B, C, and H were then evaluated after STF testing at 950°C and approximately 1% strain. In all three materials, the larger intragranular M(C,N) carbides appeared unchanged in either size or distribution — Figs. 3C, 4C, and 5C. In materials B and C there was an increase in the number of chromium-rich $M_{23}C_6$-type carbides observed along grain boundaries after STF testing — Figs. 3D and 4D. Almost all of the boundaries in material B were decorated with the intergranular carbides with some of the carbides displaying a slightly elongated morphology. In material C, the distribution of intergranular carbides was not as consistent as in material B and some boundaries remained free of carbides. In material H, some $M_{23}C_6$ precipitation was observed (Fig. 5C) but these carbides were not as apparent as in materials B and C.

In both materials B and C, a significant number of new carbides precipitated on the grain boundaries when the samples were strained at temperature during STF testing. STF samples that were heated to 950°C, and not strained, precipitated significantly fewer new carbides. This distinction becomes important when evaluating strained samples or real multipass weldments for the presence of intergranular carbides as the carbides may not have been present prior to strain. In material B there were more intergranular carbides before STF testing and are believed to have provided resistance to boundary sliding, contributing to the improved DDC resistance observed in this alloy.

Boron is known to increase the thermodynamic phase stability and precipitation kinetics of $M_{23}C_6$ and boron segregation to grain boundaries likely contributed to the improved stability of $M_{23}C_6$ over MC in material B (Refs. 32, 33). JMatPro-Ni calculations of equilibrium phase stability for the material B composition with different boron levels is shown in Fig. 6 and is consistent with the microstructural observations for materials B and C. By "engineering" the boron- and carbide-forming elements in these alloys, an improvement in DDC resistance appears to be achievable through the controlled precipitation of $M_{23}C_6$ along migrated grain boundaries in the as-welded microstructure. To further investigate this effect, tests to alter the grain boundary carbides were designed using a combination of heat

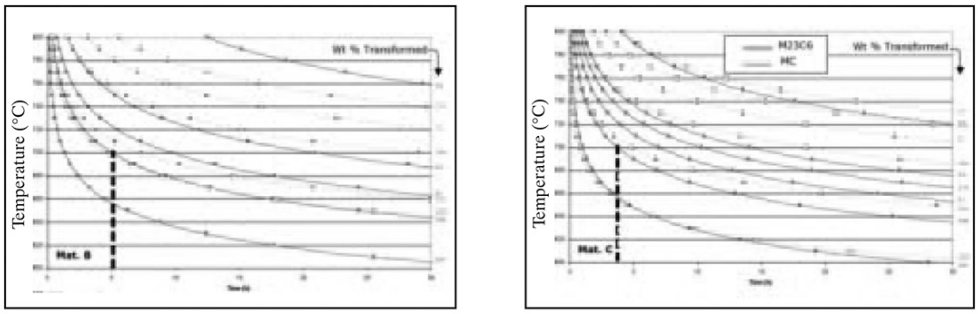

Fig. 8 — Series of overlaid TTT curves for materials B and C showing percent transformed for MC and $M_{23}C_6$ precipitates for different times and temperatures.

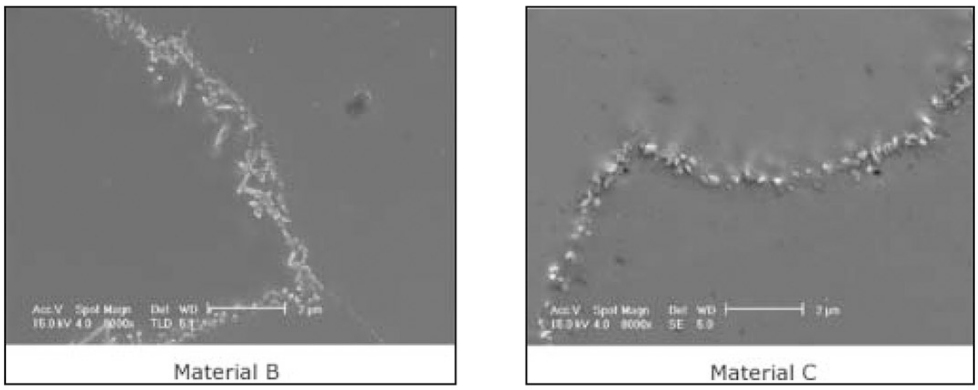

Fig. 9 — $M_{23}C_6$ carbide precipitation in materials B and C after a solutionizing heat treatment (1275°C for 1 min) followed by a precipitation heat treatment (700°C for 5 and 3.75 h, respectively).

treatment and controlled deformation.

Deformation

Carbide Engineering and Microscopic Boundary Pinning

To better understand how strain is accommodated within each material and how it is affected by the starting microstructure, EBSD scans of materials B and C were performed before and after STF testing (Ref. 5). EBSD GROD (grain reference orientation deviation) plots are developed using EBSD orientation data to evaluate the orientation relationship within a given grain. By calculating the average orientation within the grain and assigning a color gradient to graphically show deviations from that average orientation (0 deg blue, 4 deg green, 8 deg yellow, 12 deg orange, 16 deg red), a better understanding of how the grain is accommodating strain was obtained. For example, if an area within a grain of a before-STF plot is blue and the same area of the after-STF plot is yellow, this area has the same relative misorientation and therefore deformed together. However, areas within a grain that were originally all blue, but after deformation now include a transition from blue to yellow, have presumably deformed at the location of the transition. Since most of the as-welded scans were primarily blue with 10–25% green (Ref. 5), misorientation transitions from blue to yellow or green to yellow in the after-STF scans can be assumed to be the result of deformation at the color transitions. It is important to remember that since the average orientation is recalculated for each grain (outlined with black lines that define >10-deg point-to-point misorientation), care should be taken when interpreting data between grains.

EBSD GROD plots in Fig. 7 were strained to 4% (±0.5%) and demonstrate the generally observed trend in materials B and C that more misorientation transitions (i.e., blue to yellow) are located near grain boundaries in material C indicating more intergranular deformation while the transitions tended to occur more within the grains in material B indicating more intragranular deformation. There are still considerable deformation gradients within individual grains of B, but they are not as localized around grain boundaries or triple points as was found in C. Additional examples of strain effects using this technique are available elsewhere (Ref. 5).

Since grain boundary $M_{23}C_6$ carbides precipitated during STF testing for both materials B and C, the difference in deformation location appears to be controlled by the $M_{23}C_6$ carbides in material B that form in the as-welded condition (before testing). The presence of these carbides is believed to cause microscopic pinning of the grain boundaries, which thereby limits grain boundary sliding and promotes intragranular deformation.

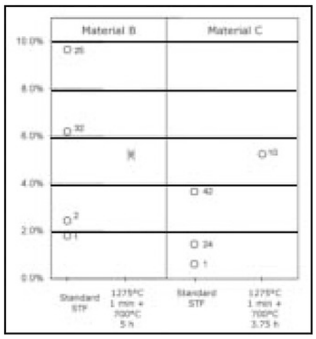

Fig. 10 — STF results for materials B and C (12.7-s downslope) heat treated at several different conditions and compared with standard STF samples (results from Fig. 2). An "x" represents a tested sample with no DDC cracking and "o" a sample with DDC cracking. The number next to the circle is the number of DDC cracks found. The two blue "x" points in material B indicate samples that dynamically recrystallized during STF testing.

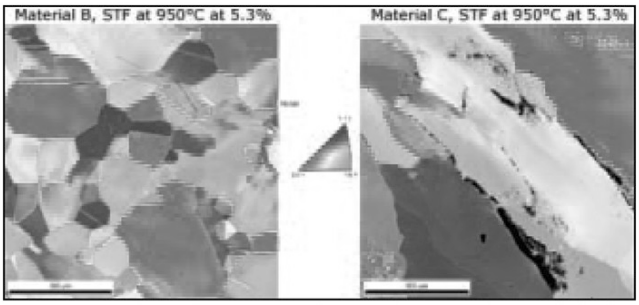

Fig. 11 — Inverse pole figure plots of EBSD data showing samples of materials B and C that had been (precipitation) heat treated and STF tested at 950°C. The recrystallized microstructure in material B had smaller grains and three (60-deg) twin boundaries throughout the structure.

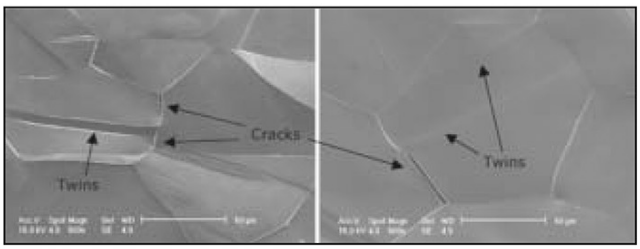

Fig. 12 — SEM image of the surface of an as-tested, dynamically recrystallized material B sample tested at 950°C and 5.3% strain where small cracks formed along the grain boundary between a triple point and a twin boundary.

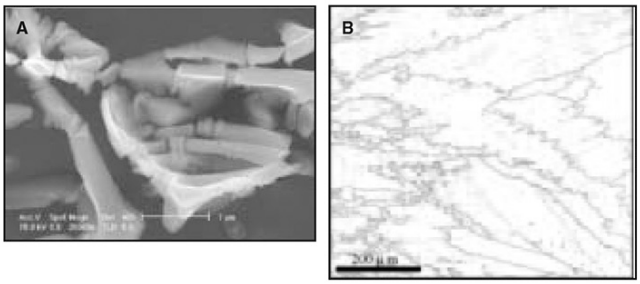

Fig. 13 — SEM image of a skeletal carbide (A) found in material H and a grain boundary map from EBSD data showing the tortuous boundaries that result (B). The 2- to 15-deg boundaries are displayed red, 15- to 55-deg and 65- to 180-deg boundaries are blue, and 55- to 65-deg boundaries are yellow.

To better understand this microscopic pinning effect by grain boundary carbides, several heat treatments were devised to alter the carbide size and distribution. Samples were tested with combinations of solutionizing and precipitation heat treatments based upon JMatPro-Ni calculations (Ref. 5). Samples of materials B and C in the as-welded condition where solution heat treated in a protective argon environment at 1275°C for 1 min to dissolve most of the carbides and then allowed to free cool (approximately 30°C/s to 1000°C and 20°C/s from 1000° to 800°C) to room temperature. The peak temperature of 1275°C was selected as it was approximately 50°C below the melting temperature of both materials B and C. Based upon several trials, a hold time of 1 min maximized the amount of MC-type carbides that dissolved without significantly affecting the grain structure. Following this heat treatment, both materials were found to have a few small (<1 µm) MN-type precipitates remaining. Consistent with the as-welded microstructures, sporadic $M_{23}C_6$ carbides formed during cooling along grain boundaries in material B but not in material C.

Following the initial solution heat treatment, samples of materials B and C were given subsequent precipitation heat treatments at 700°C for times of 5 and 3.75 h, respectively, to precipitate approximately 0.05 wt-% $M_{23}C_6$ based upon JMatPro-Ni TTT calculations shown in Fig. 8. Following the precipitation heat treatment, $M_{23}C_6$ carbides were found along grain boundaries (Fig. 9) with a greater density than observed in the standard as-welded samples — Figs. 3B and 4B. However, some of the boundaries remained relatively carbide free (<10% in material B and ~50% in material C) even after the heat treatment. The carbides in material B were generally elongated while those in material C were more symmetrical.

Subsequent STF testing of the heat-treated samples resulted in an increase in the cracking resistance of both materials B and C — Fig. 10. The STF results of material C in the precipitation heat-treated condition are similar to material B in the standard as-welded STF condition. The similarity between the grain boundary carbide distributions of these two microstructures before STF testing is in good agreement with the STF results and the microscopic boundary sliding mechanism. However, it is unclear to what extent this mechanism could be used in welds as the grain boundary carbides in these alloys become thermodynamically unstable above approximately 1100°C (Ref. 5). The kinetics of formation, therefore, becomes important in multipass welds where thermal cycles are relatively short and time to re-

form these carbides is limited.

As discussed earlier, boron plays a key role in the kinetics of dissolution and formation of the $M_{23}C_6$ boundary carbides and was found to have an effect on the DDC susceptibility in the alloys studied in this work (Ref. 1). In the materials evaluated in Part 1, increases in boron lead to an increase in the transition to gross cracking and based on the microstructure analysis of material B and C is related to the accelerated formation of intergranular $M_{23}C_6$. However, the effect that bulk composition has on the formation of different types, sizes, and morphologies of carbides and their subsequent effects on DDC in these alloys is complex and care should be taken to avoid an overly simplistic view of the boron effect. Additional work is required to further investigate the effect of boron and its interaction with other elements in these and other alloy systems (Ref. 5).

Recrystallization

The decrease in the number of cracks in the precipitation heat-treated material B samples was also accompanied by recrystallization in the spot weld during STF testing at 950°C and approximately 5% strain — Fig. 11. The recrystallization is believed to have resulted from particle-stimulated nucleation (PSN) as a result of the distribution of the elongated $M_{23}C_6$ carbides along the boundaries. To date, no other FM-52M-like alloys have recrystallized during STF testing at 950°C and while PSN is typically observed with larger precipitates (>1 μm) (Refs. 34, 35), the manner in which the $M_{23}C_6$ carbides clustered (Fig. 9) together may have reduced the critical particle size for PSN to occur (Refs. 34, 35). While no cracks were found after STF testing using the standard optical approach at 30× magnification and therefore reported as no cracking in Fig. 10, several small cracks (<50 μm) were observed along grain boundaries in the SEM — Fig. 12. When the material dynamically recrystallized, some of the new grain boundaries that formed would have been carbide free and therefore more susceptible to DDC. Any subsequent strain would lead to a DDC response similar to material C, which was relatively free of intergranular carbides in the as-welded condition. However, the resulting recrystallized microstructure formed Σ3 twin boundaries that were found to blunt subsequent DDC crack propagation — Fig. 12. This observation of crack blunting by twin boundaries is consistent with previous results (Refs. 29, 36).

Macroscopic Boundary Pinning

STF testing of material H revealed a significant resistance to DDC without the presence of $M_{23}C_6$ precipitates on grain boundaries — Fig. 2. This high resistance to DDC was attributed to the larger 1 to 5 μm skeletal carbides located throughout the microstructure. The dense distribution and large surface area of these carbides were highly effective at pinning boundaries, resulting in extremely irregular or "tortuous" boundaries — Fig. 13. This macroscopic boundary pinning has been reported previously in FM-82 alloys, although to a lesser extent (Refs. 11, 24) and acts to mechanically lock the boundaries and improves the DDC resistance by promoting intragranular deformation rather than grain boundary sliding. The macroscopic boundary locking in material H has been the most effective method for improving the DDC resistance in these FM-52M-like alloys.

Summary

The results of this work have led to the following observations regarding the effect of microstructure on DDC. Macroscopic grain boundary locking occurs when interdendritic carbides are effective at pinning grain boundaries during solidification and the resulting tortuous boundaries improve resistance by mechanical locking boundaries, resisting grain boundary sliding and subsequent DDC cracking. When strain is applied to these interlocked grains, boundary sliding becomes much more difficult due to the various boundary geometries (Fig. 13B), resulting in an increase in intragranular deformation. The effectiveness of these carbides decreases as their size, surface area, and density decrease. It should be noted that this mechanism does not improve the actual boundary strength but increases the strain required for cracking at grain boundaries (Refs. 28, 37). To date, the compositional modifications to Filler Metal 52 in material H (2.5% Nb and 4% Mo) and the resulting macroscopic grain boundary locking have been the most effective method for improving the DDC resistance in these FM-52M-type alloys.

Samples with grain boundary $M_{23}C_6$ carbides that formed before STF testing were more resistant to cracking when compared to samples that were free of grain boundary carbides. This appears to be due to microscopic grain boundary locking where the presence of carbides along the boundary increases the resistance to grain boundary sliding, leading to increased intragranular deformation. Even a moderate number of these carbides in the as-welded condition appears to increase the cracking resistance and may be sufficient in some applications where overall weld restraint is low. Since these intergranular carbides form in the solid state and often appear only after straining at temperature, their presence in a cracked sample may not indicate they formed before cracking or were beneficial in any way. The effectiveness of this mechanism is largely dependant upon the carbide dissolution and precipitation kinetics. Boron appears to be effective in this regard by increasing the stability of the carbides and may also contribute to the observed elongated morphology that was observed in material B. While not as effective as the macroscopic boundary locking mechanism, alloy optimization through this mechanism may be useful in applications where heat-to-heat composition variations produce inconsistent DDC results and even a small increase in DDC resistance (1–2% strain) may be sufficient to avoid cracking.

Certain carbide distribution and morphologies could lead to recrystallization by PSN (Refs. 34, 35, 38) resulting in a smaller grain size, dislocation annihilation, and Σ 3 twin boundaries; all of these increase the resistance to cracking. Even if complete recrystallization does not occur, partial recrystallization (the formation of some new grains along previous grain boundaries) would effectively break up the continuous crack path and improve resistance by eliminating long and straight boundaries. The effectiveness of these observations appears to be directly related to the quantity and morphology of the intergranular carbides. It has been proposed that the onset of ductility recovery at the higher temperature range of the ductility-dip temperature range is the result of recrystallization (Refs. 6, 9–11, 39). These PSN recrystallization results are consistent with the increased DDC resistance in those observations, that is, recrystallization results in an increase in ductility. However, in the case of PSN in Alloy B, recrystallization will only occur one time as the precipitates along the grain boundary that are required for PSN, only formed with an extended heat treatment. Further work is required to determine if the PSN mechanism may be reduced to practice as no filler metal compositions tested to date have produced the required grain boundary carbides in the as-welded condition.

The increase in the DDC resistance observed in material B appears to be related to the precipitation of $M_{23}C_6$ carbides in the as-welded condition — Fig. 3B. There is no evidence of a deleterious effect that may be caused by the subsequent precipitation of intergranular carbides that precipitate during straining — Fig. 3D. As such, the results of this work support a mechanism for DDC in these alloys that is associated with grain boundary sliding and the ability of intergranular $M_{23}C_6$ carbides to resist sliding, as opposed to the precipitation-induced cracking mechanism proposed by Young et al. (Ref. 8).

Conclusions

The results of this work have led to the following conclusions regarding the mechanisms that affect susceptibility to ductility dip cracking (DDC) in high-chromium Ni-based alloys.

1. Microscopic grain boundary pinning by intergranular carbides improved DDC resistance in the STF test when the carbides are present along migrated grain boundaries in the weld metal prior to the application of the strain.

2. Macroscopic grain boundary pinning by MC carbides that form at the end of solidification was found to prevent the migration of grain boundaries and resulted in tortuous boundaries that significantly improve resistance to DDC.

3. Precipitate engineering via heat treatment resulted in dynamic recrystallization by PSN and Σ3 twin boundary formation that improve the resistance to DDC.

4. DDC is an elevated-temperature grain boundary sliding mechanism. Such sliding can be opposed macroscopically by the formation of tortuous grain boundaries via a grain boundary pinning mechanism. Grain boundary sliding can also be reduced by the formation of grain boundary carbides in the solid state through appropriate alloying or by heat treatment.

Acknowledgments

The authors would like to thank Sam Kiser of Special Metals Welding Products Company (SMWPC), Dr. Suresh Babu of The Ohio State University, Dr. Morgan Gallagher (now with Acute Technologies, Inc.), Kenny Izor (now with Pratt and Whitney), and Dr. Ray Unocic from The Ohio State University for their assistance and insight during the course of this investigation. Thanks also to SMWPC for supplying filler metals and sample blanks used in some of the testing. Partial financial support for the project was provided by BWXT, Inc.

References

1. Nissley, N. E., and Lippold, J. C. 2008. Ductility-dip cracking susceptibility of nickel-based weld metals, Part 1: Strain-to-fracture testing. *Welding Journal* 87(10): 257-s to 264-s.

2. Nishimoto, K., Mori, H., and Hongoh, S. 1999. Effect of sulfur and thermal cycles on reheat cracking susceptibility in multi-pass weld metal of Fe-36% Ni alloy. IIW Doc. IX-1934-99.

3. Nishimoto, K., Saida, K., and Okauchi, H. 2006. Microcracking in multipass weld metal of Alloy 690, Part 1 – Microcracking susceptibility in reheated weld metal. *Science and Technology of Welding and Joining* 11(4): 455–461.

4. Lippold, J. C., and Ramirez, A. J. 2004. Insight into the mechanism of ductility dip cracking. IIW-IX-2123-04. Osaka, Japan.

5. Nissley, N. E. 2006. Intermediate temperature grain boundary embrittlement in nickel-base weld metals. *Welding Engineering*. The Ohio State University: Columbus, Ohio. p. 204, *www.ohiolink.edu/etd/view.cgi?acc_num=osu1156949345*.

6. Zhang, Y. C., Nakagaw, H., and Matsuda, R. 1985. Weldability of Fe-36%Ni alloy (Report V). *Transactions of JWRI* 14(2): 119–124.

7. Dix, A. W., and Savage, W. F. 1971. Factors influencing strain-age cracking in Inconel X-750. *Welding Journal* 50(6): 247-s to 252-s.

8. Young, G. A., et al. 2008. The mechanism of ductility dip cracking in nickel-chromium alloys. *Welding Journal* 87(2): 13.

9. Nissley, N. E. 2002. Development of the strain-to-fracture test to study ductility-dip cracking in austenitic alloys. *Welding Engineering*. The Ohio State University: Columbus, Ohio. p. 104.

10. Rhines, F. N., and Wray, P. J. 1961. Investigation of the intermediate temperature ductility minimum in metals. *Transactions of the ASM* 54: 117–128.

11. Ramirez, A. J., and Lippold, J. C. 2004. High temperature behavior of Ni-base weld metal. II. Insight into the mechanism for ductility dip cracking. *Materials Science & Engineering A* 380(1–2).

12. Ramirez, A. J., and Lippold, J. C. 2004. New insight into the mechanism of ductility dip cracking in Ni-base weld metals. *1st International Workshop, Hot Cracking Phenomena in Welds*. Springer-Verlag: Berlin, Germany. pp. 19–41.

13. Haddrill, D. M., and Baker, R. G. 1965. Microcracking in austenitic weld metal. *British Welding Journal* 12(9).

14. Zhang, Y. C., Nakagawa, H., and Matsuda, F. 1985. Weldability of Fe-36%Ni Alloy (Report VI). *Transactions of JWRI* 14(5): 125–134.

15. Lin, W., and Cola, M. J. 1997. Weldability of Inconel filler metal 52. *78th American Welding Society Annual Meeting, Abstracts of Papers*. April 13–17, 1997. Los Angeles, Calif.

16. Collins, M. G., and Lippold, J. C. 2003. An investigation of ductility dip cracking in nickel-based filler metals — Part I. *Welding Journal* 82(10): 288-s to 295-s.

17. Collins, M. G., Lippold, J. C., and Kikel, J. M. 2003. Quantifying ductility-dip cracking susceptibility in nickel-base weld metals using the strain-to-fracture test. *6th International Conference: Trends in Welding Research*. Pine Mountain, Ga.: ASM. pp. 586–590.

18. Nishimoto, K., et al. 2006. Microcracking in multipass weld metal of Alloy 690, Part 2 — Microcracking mechanism in reheated weld metal. *Science and Technology of Welding and Joining* 11(4): 462–470.

19. Nishimoto, K., et al. 2006. Microcracking in multipass weld metal of Alloy 690, Part 3 – Prevention of microcracking in reheated weld metal by additions of La to filler metal. *Science and Technology of Welding and Joining* 11(4): 471–479.

20. Capobianco, T. E., and Hanson, M. E. 2005. Auger spectroscopy results from ductility dip cracks opened under ultra-high vacuum. *7th International Conference: Trends in Welding Research*. Callaway Gardens Resort, Pine Mountain, Ga.: ASM International. pp. 767–772.

21. Matsuda, F. 1984. Weldability of Fe — 36% Ni alloy. II. — Effect of chemical composition on reheated hot cracking in weld metal. *Trans. JWRI* 13(2): 241–247.

22. Ramirez, A. J., Sowards, J. W., and Lippold, J. C. 2005. Effect of Nb and Ti on the ductility dip cracking of Ni-base alloys weld metal. *60th Annual ABM International Congress*. Belo Horizonte-MG, Brazil, July.

23. Kikel, J. M., and Parker, D. M. 1998. Ductility dip cracking susceptibility of filler metal 52 and Alloy 690. *Trends in Welding Research*. June 1–5, 1998. Pine Mountain, Ga. pp. 757–762.

24. Collins, M. G., Ramirez, A. J., and Lippold, J. C. 2004. An investigation of ductility-dip cracking in nickel-based weld metals — Part III. *Welding Journal* 83(2): 39-s to 49-s.

25. Lippold, J. C., and Nissley, N. E. 2006. Further investigations of ductility-dip cracking in high chromium, ni-base filler metals. *59th Annual Assembly of the International Institute of Welding*. Quebec City, Canada.

26. Ramirez, A. J., and Lippold, J. C. 2004. High temperature behavior of Ni-base weld metal. I. Ductility and microstructural characterization. *Materials Science & Engineering A* 380(1-2).

27. Nissley, N. E., and Lippold, J. C. 2005. Ductility-dip cracking susceptibility of filler metal 52 and 52M Ni-base filler metals. *Proceedings of the 7th International Conference, Trends in Welding Research VII*. Pine Mountain, Ga.: ASM International. pp. 327–332.

28. Lippold, J. C., and Nissley, N. E. 2008. Ductility dip cracking in high-Cr Ni-base filler metals. *Hot Cracking Phenomena in Welds II*, ISBN 978-3-540-78627-6: Springer. pp. 409–426.

29. Dave, V. R., et al. 2004. Grain boundary character in Alloy 690 and ductility-dip cracking susceptibility. *Welding Journal* 83(1): 1-s to 5-s.

30. Nissley, N. E., et al. 2002. Development of the strain-to-fracture test for evaluating ductility-dip cracking in austenitic stainless steels and Ni-base alloys. *Welding in the World* 46(7/8): 32–40.

31. Gerhold, R. CEOF. 2006 cited; available from *www.ceof.ohio-state.edu/*.

32. Richards, N. L., and Chaturvedi, M. C. 2000. Effect of minor elements on weldability of nickel base superalloys. *International Materials Reviews* 45(3): 109–129.

33. Czyrska-Filemonowicz, A., et al. 2003. The role of boron in the 9% chromium steels for steam power plants. *Parsons 2003: Sixth International Charles Parsons Turbine Conference*. Dublin, Ireland. pp. 365–377.

34. Humphreys, F. J. 1977. The nucleation and recrystallization at second phase particles in deformed aluminum. *Acta Metallurgica* 24: pp. 1323–1344.

35. Humphreys, F. J., and Hatherly, M. 2004. *Recrystallization and Related Annealing Phenomena*. 2nd ed. 2004, Amsterdam; Boston: Elsevier. 628 p.

36. Qian, M., and Lippold, J. C. 2003. The effect of annealing twin-generated special grain boundaries on HAZ liquation cracking of nickel-base superalloys. *Acta Materialia* 51(12): 10.

37. Lippold, J. C., and Nissley, N. E. 2007. Further investigations of ductility-dip cracking in high chromium, Ni-base filler metals. *Welding in the World* 51(9/10).

38. Bay, B., and Hansen, N. 1979. Initial stages of recrystallization in aluminum of commercial purity. *Metallurgical Transactions A* 10A: 279–288.

39. Collins, M. G. 2002. *An Investigation of Ductility Dip Cracking in Nickel-Base Filler Materials*. The Ohio State University, p. xix, 240 leaves.